Broadband operation of an InP optical phased array

Broadband Operation of an InP Optical Phased Array

M. Gagino, M. B. J. van Rijn, E. A. J. M. Bente, *Member, IEEE*, M. K. Smit, *Fellow, IEEE*, and V. Dolores-Calzadilla

***Abstract*— We demonstrate the broadband operation and beam calibration over 70nm tuning range of an optical phased array (OPA) fabricated in a generic InP photonic integration platform, which enables multi-wavelength OPA operation. The broadband performance was demonstrated on an 8-channel OPA, whose calibration and phase modulator characterization were executed through near-field and far-field measurements. The architecture reported here is scalable, and the results are promising for reducing the complexity of calibration and control of large-scale OPAs for their use at multiple wavelengths, for example, for spectral imaging or 2D beam steering through dispersive gratings.**

***Index Terms*— Beam steering, Indium Phosphide photonics, LiDAR, optical phased array, photonic integrated circuits.**

I. Introduction

OPTICAL phased arrays (OPAs) have attracted significant interest due to the beam shaping and steering capabilities for use in remote sensing and free-space communications. Because of their ability to form steerable beams in free space without moving parts, solid state OPAs offer several advantages compared to mechanical-based steering [1] and MEMS-based scanners [2] such as scalability, scanning speed, miniaturization, potential for cost reduction and reliability [3]–[5]. Within the scope of LiDAR sensing applications, the combination of OPA beam steering and the Frequency-Modulated Continuous-Wave (FMCW) technique has gained popularity to achieve a fully solid-state LiDAR system able to detect simultaneously distance and speed [6]. Generic photonic integration platforms based on InP offer the possibility to pursue such LiDAR chips by monolithically integrating active and passive components which emit in the eye-safe C-band. Moreover, voltage driven phase modulators allow high speed and energy efficient beam steering, while the integration of semiconductor optical amplifiers (SOAs) for extended detection range and on-chip tunable laser sources is possible [7], [8].

OPAs are often operated in a broadband way in applications such as spectral imaging [9] and 2D beam steering for LiDAR sensing. In particular, to achieve the latter, electrically-controlled OPA-based 1D beam steering is used alongside wavelength-dependent grating-based steering [3]. In this approach, a wide-range tunable laser (typically 50-100nm) is used, and its design and implementation were demonstrated in generic photonic integrated circuit (PIC) platforms with tuning ranges as high as 74nm [10]. However, the calibration of phased arrays and their control are wavelength dependent, and therefore having an OPA with wavelength insensitive operation is beneficial to reduce the driving complexity and to operate the OPA at multiple wavelengths. To this aim, the OPA design should be such that the optical paths in the array arms are balanced, while the wavelength dependence of its building blocks should have a negligible effect on the OPA performance.

In this letter we present the scalable design of a broadband OPA based on an InP generic photonic integration platform, which can be operated at any wavelength in a 70nm tuning range, after calibration at the central wavelength. Furthermore, we demonstrate the OPA calibration strategy, and the comprehensive characterization of the OPA phase modulators to accurately predict the array behavior in the tuning range. Finally, we demonstrate experimentally the broadband operation of the OPA, and beam steering.

II. Design of the OPA

An 8-channel OPA (Fig. 1) was designed in the *Nazca Design* software with the goal of characterizing the broadband operation while keeping the electrical control of the chip simple and easy to test via wire-bonding assembly. The chip was fabricated in the InP generic platform of SMART Photonics on an n-doped substrate. The OPA comprises three building blocks: a star coupler power splitter, 8 optically identical array arms each containing an electro-optic phase modulator (EOPM), and a densely spaced array of output waveguides that emit light into free space via cleaved anti-reflection coated facets. Two sets of wire-bonding pads were designed for redundancy. The design choices for the OPA building blocks are discussed below.

A. Star Coupler

The star coupler offers a compact and scalable solution to split the power in several channels with limited footprint, low

Manuscript received January 30, 2022; revised April 5, 2022; accepted April 28, 2022. Date of publication May 3, 2022; date of current version May 9, 2022. This work was supported by the Electronic Components and Systems For European Leadership Joint Undertaking (ESCEL JU) Project NewControl under Grant 826653-2. *(Corresponding author: M. Gagino.)*

M. Gagino, M. B. J. van Rijn, E. A. J. M. Bente, and M. K. Smit are with the Department of Electrical Engineering, Eindhoven Hendrik Casimir Institute, Technical University of Eindhoven, 5612 AP Eindhoven, The Netherlands (e-mail: m.gagino@tue.nl; m.b.j.v.rijn@tue.nl; e.a.j.m.bente@tue.nl; m.k.smit@tue.nl).

V. Dolores-Calzadilla is with the Department of Electrical Engineering, Eindhoven Hendrik Casimir Institute, Technical University of Eindhoven, 5612 AP Eindhoven, The Netherlands, and also with the Photonic Integration Technology Center, 5612 AP Eindhoven, The Netherlands (e-mail: v.calzadilla@tue.nl).

Color versions of one or more figures in this letter are available at https://doi.org/10.1109/LPT.2022.3171979.

Digital Object Identifier 10.1109/LPT.2022.3171979

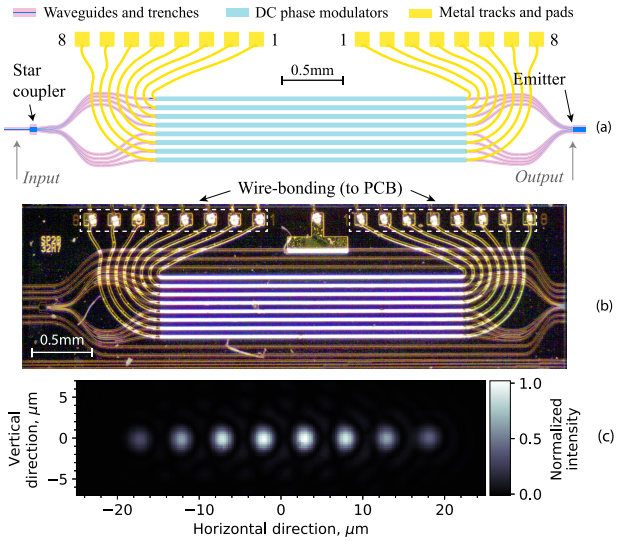

Fig. 1. (a) Schematic of the 8-channel optical phased array and (b) microscope picture of the fabricated chip. (c) Near-field image of the emitter waveguides showing the intensity of the fundamental TE-modes (i.e., polarized along the horizontal direction).

insertion losses, and small wavelength dependence. For the OPA described in this work, we predicted analytically the star coupler behavior by assuming a Gaussian mode profile of the input waveguide and a Gaussian beam propagation towards the array waveguides. We estimated a non-uniformity (i.e., power variation between the inner channels and the outer channels) of 2.7dB and an insertion loss of 2.3dB for the designed star coupler which has a radius of $62.5\mu m$, $1.5\mu m$-wide deep-etched waveguides, and $2.3\mu m$ array pitch. For 100nm tuning range, the model predicts variations in non-uniformity and insertion loss of 0.04dB and 0.01dB respectively.

B. Electro-Optic Phase Modulators

The EOPMs in our OPA design are deep-etched waveguides with a bulk core material. They are operated in reverse bias and have a baseline efficiency of $15°V^{-1}mm^{-1}$ for TE polarized light at 1550nm wavelength [7], [8]; a length of 2.5mm was chosen to achieve $V_{2\pi} < 10V$. The EOPMs have a near linear phase-voltage relation, with a small quadratic component [11], [12]. Their insertion loss is voltage and wavelength dependent due to electro-absorption.

C. OPA Emitter

The emitter section used in this PIC is a periodic array of $1.5\mu m$-wide deep-etched waveguides with a pitch of $5\mu m$. The pitch guarantees negligible optical crosstalk between channels and provides a field of view (FoV, i.e., the range of steering angles before the main beam and the grating beam become indistinguishable) of 17.8° at 1550nm. Since we are interested in a scalable design, all the waveguides in the OPA are deep-etched because of their smaller bending radius ($100\mu m$) compared to shallow-etched waveguides ($400\mu m$), which minimizes the OPA footprint. Moreover, the strong mode confinement of deep-etched waveguides minimizes optical crosstalk between them, which is helpful to achieve a wide-FoV angular steering.

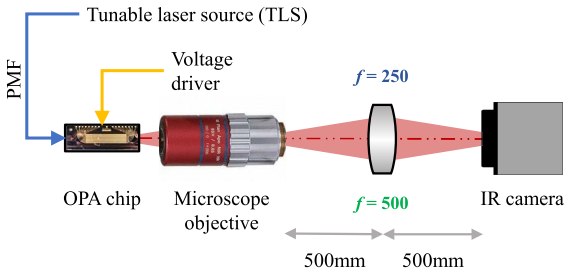

Fig. 2. Schematic of the measurement setup. Two different lenses are used to image the near-field ($f_{NF} = 500mm$) and far-field ($f_{FF} = 250mm$).

For this OPA design, the simulated angular resolution is 2.1° at 1550nm, the image resolution (number of resolvable spots in the FoV) is 8, and the diffraction sidelobes suppression ratio (SSR) is −15.4dB; within the FoV of the OPA, 76% of power is expected to be confined within the full-width at half maximum (FWHM) of the main beam. These results were obtained through simulations of the mode and through far-field propagation using *Lumerical MODE* and *FDTD* solvers.

III. OPA Characterization and Calibration

A. Characterization Setup

In order to characterize the fabricated device, the PIC was wire-bonded to a PCB. The OPA characterization was carried out with a free space setup, as depicted in Fig. 2. An infrared microscope objective with a numerical aperture NA = 0.42 and a focal length of 4 mm was used to collimate the light emitted from the OPA. The near-field image of the emitter was projected onto the infrared camera (*Xenics Xeva 320*, 30 μm pixel size) through a lens with 500 mm focal length. The far-field was imaged with a 250 mm focal length lens which was placed in the same position. The near-field magnification factor was $M = 500mm/4mm = 125$, giving a resolution of $0.24\mu m$ per pixel; the measured far-field resolution was 0.46° per pixel. A *NI cDAQ 9264* voltage driver provided the bias to the EOPMs, and light from a tunable laser source (*HP 8168A*, tuning range 70nm) was coupled to the PIC by means of a polarization-maintaining fiber (PMF) which excited the TE fundamental mode.

B. OPA Characterization

We characterized the non-uniformity of the star coupler building block by imaging the near-field of the OPA emitter and measuring the relative optical intensity of the waveguide modes (Fig. 1c). We derived a non-uniformity of 5dB. The deviation from the design value is attributed to a measured 20% fabrication tolerance in the input waveguide width and to the precision of the Gaussian approximation used in the design of the star coupler.

We characterized the voltage and wavelength dependent loss variations in the EOPMs by sweeping the reverse bias voltage in each arm of the OPA from 0V to 10V in steps of 0.2V, and recording the peak intensity in the modes through near-field imaging (Fig. 1c). We thus obtained the excess loss curves shown in Fig. 3b (right axis) after fitting the measurement results with a quadratic polynomial ($EL(V) = 1 - l_1 V + l_2 V^2$) which accounts for the decrease of loss for voltages lower

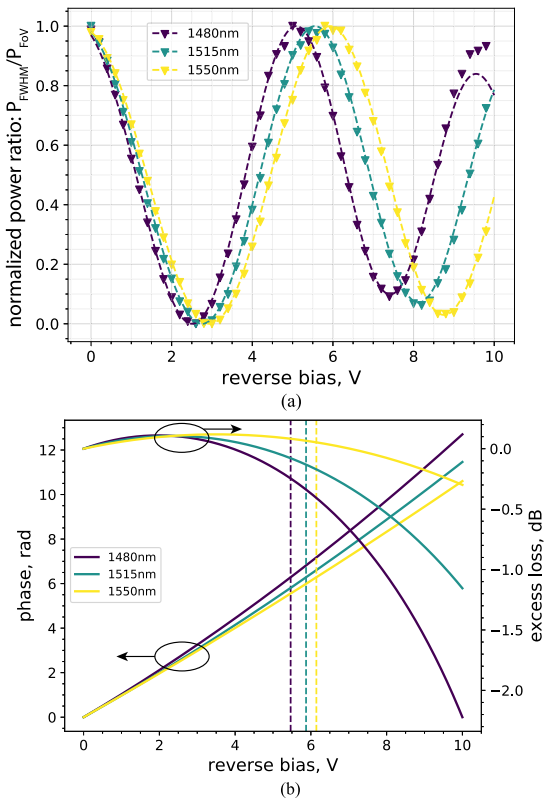

Fig. 3. Calibration and characterization of OPA channel #1; all channels displayed a similar performance. (3a) Measured data (triangles) and fit function (dashed lines) of the power ratio R. The minimum value of R is subtracted from the data, which is then normalized with respect to the maximum value of R to highlight the EOPMs voltage and wavelength dependence. (3b, left axis) Phase response to reverse bias voltage in the EOPM: $\phi(V)$. The dashed lines show the $V_{2\pi}$ voltage at each wavelength. (3b, right axis) Fit function of the EOPM excess loss.

than $\sim 5V$ due to carrier-depletion effects and its increase at higher voltages due to field effects [11]. As Fig. 3b shows, the measured excess loss of EOPMs in the designed OPA, for the tuning and bias range of interest is below -2.25dB. The measured propagation loss of deep-etched waveguides is 1.6dB/cm.

C. OPA Calibration Method

Variations in waveguide dimensions due to fabrication tolerances are responsible for random phase variations along the length of passive waveguides on the chip [13]. This results in a non-uniform phase front at the edge of the chip in the absence of phase control. We employed the modified Rotating Element Electric Field Vector (mREV) method [14], [15] to calibrate the OPA against the phase offsets in the arms. In the mREV method each channel is independently calibrated by measuring its interference pattern with the rest of the array in the far-field at a given angle. The practical implementation of the method consists in consecutively calibrating each arm by sweeping the EOPM's reverse bias voltage and measuring the power ratio R between the main peak (within the FWHM) and the FoV: $R = P_{FWHM}/P_{FoV}$. This voltage dependent quantity is an indication of the quality of the beam during calibration and it is maximum at the bias point for which the calibrated arm is in phase with the rest of the array. Fig. 3a shows the measured power ratio R for one channel of the OPA at three different wavelengths in the tuning range; the channel is calibrated for voltages between $5V$ and $6V$.

Furthermore, it is possible to extract the voltage and wavelength dependent phase relation of the EOPMs by fitting the measured power ratio R with Eq. 1, which describes the interference of light from one channel, being modulated in phase and amplitude, with the radiation from the array.

$$R_{fit}(V) = a_0 + a_1^2 + (a_2 L_a)^2 + 2a_1 a_2 L_a cos(\phi(V)) \quad (1)$$

In Eq. 1, a_0 is the background signal recorded by the camera, a_1 is the amplitude level caused by the arms with a fixed voltage, a_2 is the amplitude of the arm being calibrated, which is corrected by an amplitude term $L_a(V)$ for the EOPM's excess loss. The phase $\phi(V) = \phi_0 + \phi_1 V + \phi_2 V^2$ is described by three parameters: ϕ_0 is the phase offset of the OPA arm, ϕ_1 is the linear phase efficiency of the EOPMs, and ϕ_2 is the phase quadratic term. We extracted the EOPMs phase-voltage relation shown in Fig. 3b (left axis) by fitting the power ratio measurement of Fig. 3a with Eq. 1. From the fit, we obtained the EOPMs $V_{2\pi}$ periods which are between 5.5V and 6.1V in the 70nm tuning range, giving a 2π efficiency of 1.14rad/V$-$1.03rad/V. The measured efficiency is higher than the expected baseline of $15°V^{-1}mm^{-1}$ and we attribute this difference to a biasing of the waveguides connected to the phase modulators, which leads to an increase of the effective modulator length.

IV. Broadband Far-Field Response

In order to define the quality of the beam after calibration, we analyzed the OPA far-field camera image and we compared it to the simulation results of an array with identical emitter parameters. Fig. 4a shows the measured 1D horizontal cross section of the far-field image at 1550nm wavelength. The measurement fits well with the model predictions: we measured an angular resolution (FWHM) of 2.48° giving an image resolution of 7 points, and a SSR of -12.8dB. 70% of the power available in the FoV region (i.e., shaded area in Fig. 4a) is in the main beam's FWHM. The broadband behavior of the OPA was characterized by measuring the same properties across the tuning range (Fig. 4b), while only using the calibration dataset obtained at 1515nm. The measurement results show that the beam power level is stable across 70nm tuning range with 69%$\pm$3.5% of the power located in the main beam and a sidelobe suppression of -11.7dB$\pm$1.8dB. Further, we measured an angular resolution of 2.48°$\pm$0.3°. Small fluctuations of the parameters are attributed to non-idealities of the measurement setup, such as imperfect alignment, stray light from the chip substrate and limited camera resolution. The EOPM quadratic phase term wavelength dependence also contributes to the beam deterioration. In each channel, its effect is limited to $< 0.5rad$ variations in the $(0, V_{2\pi})$ bias range.

Finally, to demonstrate the applicability of the calibration results for beam steering and their accuracy, we swept the beam within the OPA field of view at the 1515nm central wavelength (Fig. 5). No degradation of the beam properties is observed during steering: the measured angular resolution, power ratio R, and SSR are 2.37°$\pm$0.07°, 68%$\pm$2.3%, and

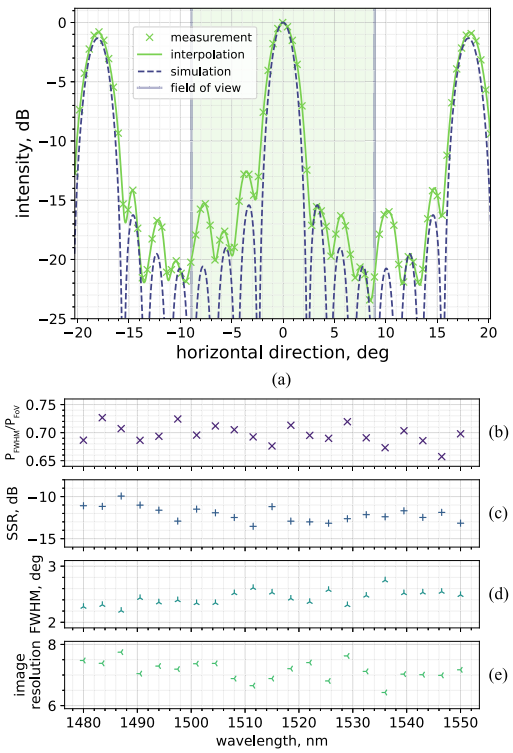

Fig. 4. (4a) Far-field of the calibrated OPA at 1550nm (green crosses are measurement points and the green solid line is an interpolation with a cubic spline). The measurement is compared to a simulated far-field (blue dashed lines). The shaded green area shows the FoV region within which R is calculated. (4b) Power ratio R, (4c) sidelobes suppression ratio, (4d) angular resolution, and (4e) image resolution for 21 wavelengths in the tuning range.

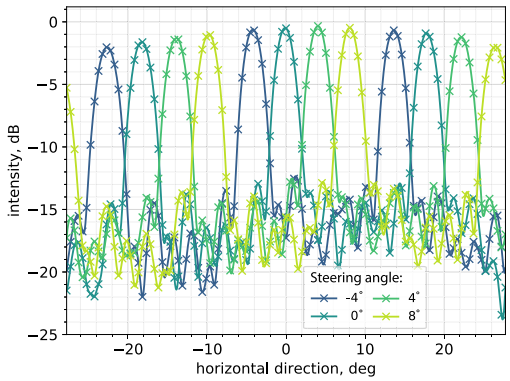

Fig. 5. Beam steering at the central wavelength, 1515nm, at different steering angles. Measured data (crosses) and interpolation (solid lines) are shown.

−12.3dB±0.7dB, respectively. The OPA modulators were controlled with voltages lower than $V_{2\pi}$, giving negligible excess loss (<0.2dB). Beam steering at wavelengths within the 70nm range showed a similar behavior.

V. Conclusion

We demonstrated a broadband 8-channel optical phased array in an InP generic photonic integration platform. The star coupler for power splitting, and the balanced optical paths ensure that a 70nm tuning range around the 1515nm central wavelength can be achieved with stable power in the main beam and negligible variations of the far-field properties. Our measurements showed in fact that the power within the FWHM of the main beam is 69% of the total power in the FoV, with ±3.5% variations in the wavelength range. Furthermore, we measured an SSR of −11.7dB±1.8dB, and an angular resolution of 2.48°±0.3°, resulting in 7 resolvable spots across the tuning range. The measurement results are compliant with the simulations results, with some variations due to non-idealities in the measurement setup.

By using a mREV calibration method, we showed that a complete characterization of the OPA can be done through measurements of the near-field and far-field. The phase-voltage relation in the EOPMs can be extracted with accuracy, resulting in negligible variations of the beam far-field properties during angular steering, while the voltage-dependent excess loss is negligible in the bias and tuning range of interest.

The broadband performance is promising for reducing complexity of calibration and control of 2D beam steering based on wavelength tuning and dispersive gratings. Future directions of our OPA research may include adding a grating for 2D beam steering, integrating SOAs for power boosting and amplitude control in the arms, and scaling up the number of channels.

Acknowledgment

The authors would like to acknowledge Michail Chatzimichailidis for wire-bonding support.

References

[1] R. Halterman and M. Bruch, "Velodyne HDL-64E LIDAR for unmanned surface vehicle obstacle detection," *Proc. SPIE*, vol. 7692, pp. 123–130, May. 2010.
[2] B. Yoo *et al.*, "A 32 × 32 optical phased array using polysilicon sub-wavelength high-contrast-grating mirrors," *Opt. Exp.*, vol. 22, no. 16, pp. 19029–19039, Aug. 2014.
[3] T. Kim *et al.*, "A single-chip optical phased array in a wafer-scale silicon photonics/CMOS 3D-integration platform," *IEEE J. Solid-State Circuits*, vol. 54, no. 11, pp. 3061–3074, Nov. 2019.
[4] K. Komatsu, Y. Kohno, Y. Nakano, and T. Tanemura, "Large-scale monolithic inp-based optical phased array," *IEEE Photon. Technol. Lett.*, vol. 33, no. 20, pp. 1123–1126, Oct. 15, 2021.
[5] Y. Guo, Y. Guo, C. Li, H. Zhang, X. Zhou, and L. Zhang, "Integrated optical phased arrays for beam forming and steering," *Appl. Sci.*, vol. 11, no. 9, p. 4017, 2021.
[6] B. J. Isaac, B. Song, S. Pinna, L. A. Coldren, and J. Klamkin, "Indium phosphide photonic integrated circuit transceiver for fmcw lidar," *IEEE J. Sel. Topics Quantum Electron.*, vol. 25, no. 6, pp. 1–7, Apr. 2019.
[7] M. Smit *et al.*, "An introduction to InP-based generic integration technology," *Semicond. Sci. Technol.*, vol. 29, no. 8, 2014, Art. no. 083001.
[8] L. M. Augustin *et al.*, "Inp-based generic foundry platform for photonic integrated circuits," *IEEE J. Sel. Topics Quantum Electron.*, vol. 24, no. 1, pp. 1–10, Jan. 2018.
[9] N. Li *et al.*, "Spectral imaging and spectral lidar systems: Moving toward compact nanophotonics-based sensing," *Nanophotonics*, vol. 10, no. 5, pp. 1437–1467, 2021.
[10] S. Latkowski *et al.*, "Novel widely tunable monolithically integrated laser source," *IEEE Photon. J.*, vol. 7, no. 6, pp. 1–9, Dec. 2015.
[11] S. Andreou, K. A. Williams, and E. A. J. M. Bente, "Steady-state analysis of the effects of residual amplitude modulation of inp-based integrated phase modulators in pound-drever-Hall frequency stabilization," *IEEE Photon. J.*, vol. 11, no. 3, pp. 1–14, 2019.
[12] M. Tahvili, "Photonic integrated circuits for shaped pulse laser systems," Ph.D. dissertation, Dept. Elect. Eng., Eindhoven Univ. Technol., Eindhoven, The Netherlands, 2013.
[13] T. Goh, S. Suzuki, and A. Sugita, "Estimation of waveguide phase error in silica-based waveguides," *J. Lightw. Technol.*, vol. 15, no. 11, pp. 2107–2113, Nov. 1997.
[14] Q. Zhang *et al.*, "An antenna array initial condition calibration method for integrated optical phased array," 2019, *arXiv:1902.06203*.
[15] S. Mano and T. Katagi, "A method for measuring amplitude and phase of each radiating element of a phased array antenna," *Electron. Commun. Jpn.*, vol. 65, no. 5, pp. 58–64, Jan. 1982.